Optical Nano-Constructs Composed of Genome-Depleted *Brome Mosaic Virus* Doped with a Near Infrared Chromophore for Potential Biomedical Applications

Bongsu Jung,[†] Ayala L. N. Rao,[‡] and Bahman Anvari*[,†]

[†]Department of Bioengineering, University of California - Riverside, Riverside, California 92521, United States, and [‡]Department of Plant Pathology and Microbiology, University of California - Riverside, Riverside, California 92521, United States

ABSTRACT We have engineered an optical nanoconstruct composed of genome-depleted *brome mosaic virus* doped with indocyanine green (ICG), an FDA-approved near-infrared (NIR) chromophore. Constructs are highly monodispersed with standard deviation of ±3.8 nm from a mean diameter of 24.3 nm. They are physically stable and exhibit a high degree of optical stability at physiological temperature (37 °C). Using human bronchial epithelial cells, we demonstrate the effectiveness of the constructs for intracellular optical imaging *in vitro*, with greater than 90% cell viability after 3 h of incubation. These constructs may serve as a potentially nontoxic and multifunctional nanoplatform for site-specific deep-tissue optical imaging, and therapy of disease.

KEYWORDS: cancer · fluorescence imaging · nanomedicine · nanotechnology phototherapy · viral capsids

In recent years, various types of nanosized structures have been developed for applications in optical imaging and therapy of disease.[1−6] Near infrared (NIR) fluorescence imaging that uses exogenous nanoconstructs is particularly advantageous in that (1) NIR wavelengths have a relatively deep optical penetration (>1 cm), (2) there is negligible tissue autofluorescence in the NIR band so that the use of an exogenous fluorophore enhances the signal to background ratio, and (3) use of nanoscale optical contrast agents can provide a technique for imaging at subcellular and molecular levels. For example, quantum dots (QDs) represent the semiconductor class of optical nanomaterials used in NIR imaging.[7−9] However, there have been reports of compromised cell viability,[10−12] possibly resulting from the liberation of ions such as Cd^{2+} with recommendations for further studies to assess the *in vivo* toxicity and degradation of QDs.[7,13,14]

Metallic materials including gold nanoparticles are another class of exogenous chromophores under investigation for both optical imaging and photothermal therapy.[15−17] Potential capabilities of gold nanoparticles in fluorescence lifetime imaging, photoacoustic imaging, and contrast enhancement during optical coherence tomography (OCT) have been reported.[18−22]

Recently, the concept of using biological materials, particularly viruses, as templates for development of platforms for imaging and therapeutic applications has gained increasing attention.[23−26] Plant viruses and recombinant adenoviruses have been investigated as potential vaccine carriers and agents in gene therapy and oncolytic viral therapy.[27−29] Inorganic materials including QDs,[30] gold,[31,32] and magnetic[33] nanoparticles have been incorporated within animal and plant viruses for imaging applications. Protein cages, assembled from the cowpea chlorotic mottle virus,[34] and the capsid of the MS2 bacteriophage have been labeled with Gd^{3+} to form novel MRI contrast agents.[35,36]

In comparison to various groups of animal viruses, plant viruses lack a lipid envelope and are especially attractive because of their ease of production and purification, and relative chemical and structural stability.[37−39] There have been several studies to conjugate organic dyes or targeting moieties onto the exterior surface of plant viruses. For example, surface conjugation of cowpea mosaic virus (CPMV) with a folic acid−PEG moiety has been demonstrated to allow specific recognition of tumor cells bearing the folate receptor *in vitro*.[40] Potato virus X

*Address correspondence to anvarib@ucr.edu.

Received for review October 24, 2010 and accepted December 24, 2010.

Published online 10.1021/nn1028696

(PVX), surface-labeled with non-NIR fluorescent OregonGreen 488 or AlexaFluor 647 dyes, has been successfully used to image mouse fibroblast and human cervical cancer cells *in vitro*.[41] In the latter study, it was demonstrated that the choice of the fluorophore influenced the fluorescent signal associated with PVX. In a recent work, the surface of RNA-containing CPMV was fluorescently labeled with AlexaFluor 555, a non-NIR fluorophore, and used for *in vivo* vascular imaging in mice and chick embryos.[42] Results of this study are extremely encouraging in that they demonstrate the potential of using a fluorescently labeled plant virus for successful *in vivo* vascular imaging.

Here, we present the first results to demonstrate encapsulation of an organic NIR chromophore into a plant virus and subsequent utilization of the construct for mammalian intracellular optical imaging. Specifically, we have engineered a nanoprobe based on genome-depleted *brome mosaic virus* (BMV), a plant ribonucleic acid (RNA) virus of alphavirus-like superfamily,[43] whose interior is doped with indocyanine green (ICG), a NIR fluorophore approved by United States Food and Drug Administration (FDA). We refer to these nanoprobes, as optical viral ghosts (OVGs) since the virions no longer contain the genomic machinery. Only the capsid protein (CP) subunits remain to encapsulate ICG.

While we have previously reported on encapsulation of ICG into synthetic polymeric nanocapsules, and their potential utility for *in vivo* optical imaging and photothermal therapy,[44−48] to our knowledge, there are no previous reports of encapsulating a NIR probe into a plant virus. Recent studies have demonstrated that encapsulation of organic dyes into structures such as lipid, silica, calcium phosphate, and polymeric nanoparticles can enhance the optical performance of the dye as assessed by increased quantum yield and fluorescent lifetime, and improved optical absorption stability.[46,49−51] Given the optical instability of free ICG when exposed to physiologically relevant conditions (*e.g.*, blood plasma and body temperature), its short vascular circulation time (plasma clearance half-life on the order of 3−5 min), and nearly exclusive uptake by the liver, encapsulation of ICG may provide a method to overcome these limitations by shielding ICG to reduce or eliminate its nonspecific interactions with plasma proteins.

In addition to being a NIR fluorophore and one of the least toxic agents administered to humans,[52] our choice of ICG is further rationalized on the basis of its physicochemical properties and its interaction with CP subunits to create self-assembled optical nanoconstructs. ICG (molecular weight (MW) = 775 Da) is composed of two polycyclic (benzoindotricarbocyanine) moieties linked with a polyene chain. Two sulfonate groups are bound to the nitrogens of the polycyclic systems *via* butylenes, resulting in net negative charge and water solubility.

The natural self-assembly and stability of plant viruses can be explained by protein−protein (*e.g.*, in CPMV) and protein−RNA interactions (*e.g.*, in BMV). In BMV, the interactions between the N- and C-termini of CP subunits contribute to form CP dimers required for the self-assembly of virions.[53,54] A positively charged arginine-rich motif in the N-terminus of a CP subunit interacts with the negatively charged phosphate group in the RNA during encapsidation.[53,55,56] RNA is likely used as the nucleating agent to initiate the self-assembly of virions.[57] It is known that the protein−RNA interaction of BMV is electrostatic and specific in nature.[43]

The nature of protein−RNA interactions can be exploited to create virus-based constructs containing genomic as well as nongenomic materials. Various RNAs without common sequences have been successfully packaged into BMV *in vitro*.[43] Inorganic materials such as negatively charged gold nanoparticles have been incorporated into BMV-based cages.[31] Contrast agents have also been functionalized to render negatively charged surfaces and proper surface conditions for successful construction of viral-based constructs. Examples include HS−PEG−COOH-coated QDs,[30] HOOC−PEG−PL-coated magnetic (iron oxide) nanoparticles,[33] carboxylate-terminated thiolalkylated tetraethylene glycol (TEG)-coated gold[31] incorporated with BMV, and mercaptoacetic acid (MAA)-coated QDs used in conjunction with simian virus 40.[58]

We capitalize on the intrinsic negative charge of ICG to initiate interactions with BMV CP subunits in a similar manner where the subunits interact with the native RNA during the virions self-assembly process. When replacing the RNA with ICG, the negatively charged ICG interacts with the positively charged arginine-rich motif in the N-terminus of BMV CP subunits to create the OVGs. In this paper, we demonstrate successful construction of genome-depleted BMV doped with ICG, characterize the optical and physical stability of the constructs, show their effectiveness in intracellular optical imaging of mammalian cells, and evaluate their cytotoxicity *in vitro* using a viability assay.

RESULTS AND DISCUSSION

Barley leaves were mechanically inoculated with purified BMV virions. Systemically infected leaves were harvested two weeks post inoculation. OVGs were constructed using a four-step process (1) virus purification from the systemically infected barley leaves, (2) virus disassembly and disassociation into capsid protein (CP) subunits, (3) separating the RNAs from CP subunits, and finally (4) replacing the RNAs with ICG, and CP reassembly to encapsulate ICG. The schematic of the steps to construct the OVGs after BMV purification is depicted in Scheme 1. Further details associated

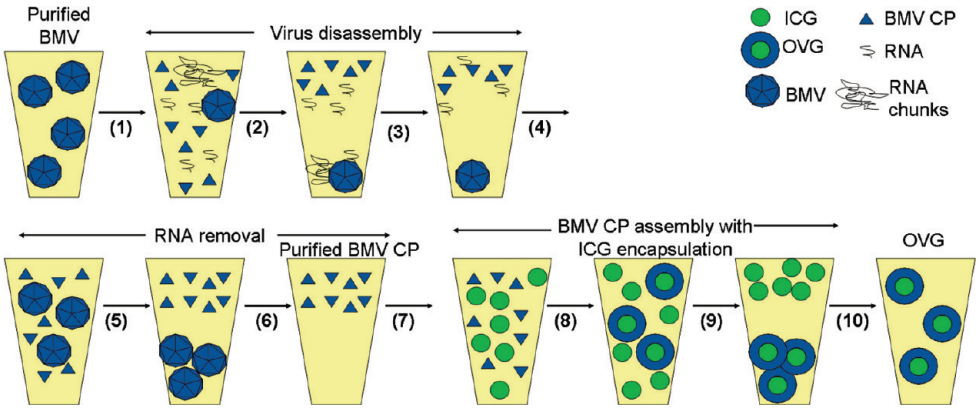

Scheme 1. Depiction of steps to create OVGs after BMV purification
(1) Dissociate the CP subunits by dialysis against disassembly buffer; (2) discard the pellet containing RNA chunks and non-dissociated BMV by low-speed centrifugation (15k revolution per minute (RPM), 30 min), and collect the dissociated CP from the supernatant; (3) discard the pellet containing undissociated BMV by high-speed centrifugation (90k RPM, 1 h), and collect the dissociated CP subunits from the supernatant; (4) remove residual RNA by dialysis against RNA assembly buffer under neutral pH condition; (5) discard the pellet (re-assembled BMV containing RNA) by high-speed centrifugation (90k RPM, 1 h); (6) collect purified dissociated BMV CP subunits from the supernatant; (7) add ICG into CP solution; (8) re-assemble BMV CP and ICG by dialysis against BMV re-assembly buffer for 24 h; (9) discard the supernatant (excess ICG) by high-speed centrifugation (90k RPM, 1 h), and collect OVGs from the pellet; and (10) resuspend OVGs with BMV suspension buffer.

with each of these steps, are provided in the Supporting Information document that accompanies this paper.

We present transmission electron microscopy (TEM) images of BMV (Figure 1a), genome-depleted BMV not impregnated with ICG (viral ghosts (VGs)) (Figure 1b), and OVGs (Figure 1c). OVGs were constructed using $\phi = 4$ where we define ϕ as the ratio of BMV CP subunits concentration to ICG concentration during reassembly. The viral particles, including OVGs, show none or very minimal aggregation (panels a−c of Figure 1). Respective diameter distributions for BMV, VGs, and OVGs are shown in panels d−f of Figure 1. The mean overall diameter of OVGs (core plus shell thicknesses), as determined from the analysis of TEM images, is ~24.3 nm (Figure 1f). It has been reported that nanoparticles in the 10−100-nm diameter range are too large to undergo renal elimination and yet too small for efficient macrophage uptake.[59,60] Since the diameter of OVGs falls within the 10−100-nm range, it is possible that they may have an optimal diameter, as a requirement, for prolonged circulation in body. OVGs also exhibit a high level of monodispersity in their size, as evidenced by the relatively low standard deviation (SD) in diameter (±3.88 nm).

To date, a number of nanoconstructs derived from nonbiological or nonprotein materials have been used to encapsulate ICG. These systems have been constructed from poly(lactide-*co*-glycolic acid) (PLGA),[61] modified silicate (ormosil) matrices using sol−gel chemistry,[62] polymeric micelles formed from poly(styrene-*alt*-maleic anhydride)-block-poly(styrene)) (PMSA-*b*-PSTY) diblock copolymers,[63] and calcium phosphate.[64] The PLGA- and ormosil-based constructs are considerably larger than OVGs with approximate mean diameters of 300 and 100 nm, respectively. PMSA-*b*-PSTY diblock copolymers and calcium phosphate-based constructs have a similar size to that of OVGs, with respective mean diameters of 30 and 16 nm. However, in contrast to all of these other constructs, formation of OVGs is mediated through a self-assembly process that utilizes viral CP subunits.

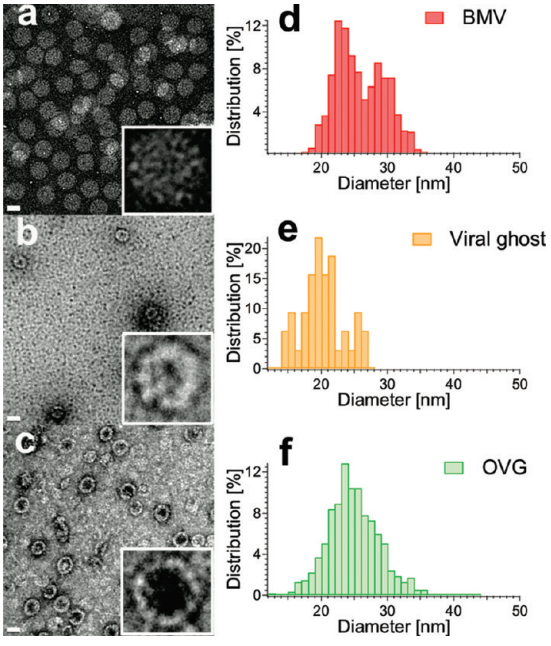

Figure 1. TEM images, and diameter distributions. Panels (a−c) correspond to TEM images of BMV, viral ghosts (VGs), and optical viral ghosts (OVGs), respectively. The scale bar is 20 nm in these panels. Insets within respective panels (a−c) show enlarged images of a BMV, VG, and OVG. Panels (d−f) correspond, respectively, to diameter distributions of BMVs, VGs, and OVGs. We constructed the OVGs using ICG concentration of 23.4 μg mL^{-1} in BMV suspension buffer solution, and ϕ = 4.

BMV capsid is composed of 12 pentamers and 20 hexamers.[65] The icosahedral morphology of BMV

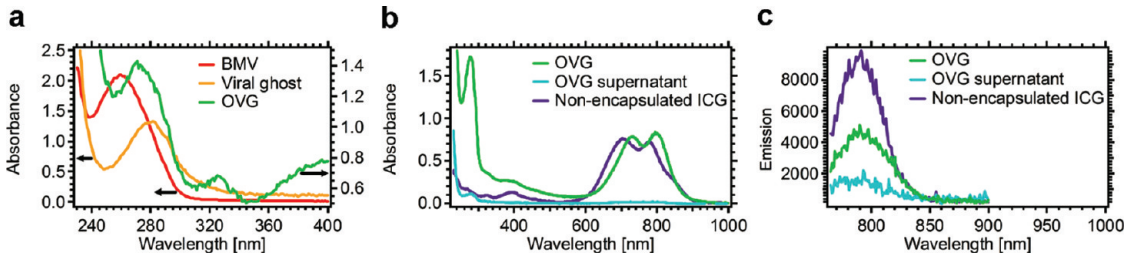

Figure 2. Optical absorption and fluorescence characteristics. In panel (a), absorption spectra for BMV, VGs, and OVGs in the UV spectral band of 230−400 nm are presented. Concentrations of BMV and VGs were 0.18 and 0.804 mg mL^{-1}, respectively. The arrows in panel (a) indicate the ordinate to which the respective spectrum corresponds. In panel (b), absorption spectra in the UV−NIR band for non-encapsulated ICG, OVG, and the OVG supernatant solution are shown. In panel (c), the fluorescence spectra in response to 750-nm excitation wavelength for non-encapsulated ICG, OVG, and the OVG supernatant solution are presented. The ICG concentration used to construct the OVGs was identical to that of nonencapsulated ICG (~10 μg mL^{-1} in BMV suspension buffer solution) with ϕ = 400.

(Figure 1a), is consistent with those reported in other literature,[65−67] and characterized as T = 3 symmetry (180 capsid subunits), where T is the triangulation number. VGs and OVGs appear as hollow spheres, and resemble a (T = 1)-like symmetry (60 subunits composed of only pentamers).[57,65] This result is consistent with previous studies, which indicate that when genome-free capsids of BMV are assembled *in vitro*, the triangulation changes from T = 3 to T = 1.[68,69] Similar T = 1 symmetry has been reported with the BMV protein cage encapsulating gold nanoparticles functionalized with polyethylene glycol (PEG).[70] Interestingly, the T = 1 symmetry is reportedly more structurally uniform and ordered than the native T = 3 virions.[65] The T = 1 like symmetry of OVGs is one indication of successful deletion of the RNA during our *in vitro* construction process.

While similar hollow spherical morphologies (T = 1) are observed for both VGs and OVGs (b and c of Figure 1), our analyses of TEM images indicate an increase in diameter of OVGs (24.3 ± 3.8 nm) (Figure 1f) as compared with that of VGs (19.7 ± 3.14 nm) (Figure 1e), suggesting that the former became successfully doped with ICG. VGs have smaller diameters than BMV (25.3 ± 3.76) (Figure 1d), which we attribute to exclusion of RNA.

We also measured the zeta (ζ)-potentials of BMVs, VGs, and OVG in deionized water. The respective values (mean ± SD) for BMVs, VGs, and OVGs were 4.4 ± 0.66, 19 ± 3.77, and 6.1 ± 0.83 mV. VGs have the largest positive ζ-potential, another indication that they are void of the negatively charged RNA. As VGs become doped with ICG (also negatively charged), the mean ζ-potential reverts back to a less positive value, closer to that associated with BMV. Particles bearing near-neutral charges are reported to be less attractive to phagocytes than those with large cationic or anionic surface charges,[71,72] suggesting that OVGs may be relatively resistant to phagocytosis.

In Figure 2, we present the absorption spectra of BMV, VGs, and OVGs in the ultraviolet (UV)−NIR spectral range (230−1000 nm). Absorption of BMV originates from both the proteins and RNAs and peaks at about 260 nm (Figure 2a), consistent with previous literature.[73] In the absence of RNA, VGs demonstrate a red-shift in peak absorption wavelength from ~260 to 280 nm (Figure 2a). With ICG loading, OVGs show a reversal in the peak absorption wavelength in the blue direction to approximately 270 nm, indicating the presence of CP subunits to encapsulate ICG.

Nonencapsulated ICG in BMV suspension buffer solution (10 μg mL^{-1}) displays the two peaks associated with the dimeric and monomeric forms of ICG, at wavelengths of 705 and 780 nm, respectively (Figure 2b). The spectrum of the supernatant collected immediately after OVG construction (Figure 2b) shows some UV absorbance, which indicates that not all the CP subunits were utilized during OVG formation process. The supernatant spectrum shows no NIR absorbance to indicate that almost the entire ICG used during the construction process became incorporated into the OVGs.

Despite the red-shifts associated with the dimeric and monomeric peaks of ICG, OVGs maintain the overall shape of the absorption spectrum of ICG in the 600−900-nm NIR range (Figure 2b), indicating that the VGs have become optically active due to ICG loading. Similar red-shifts are reported for ICG encapsulated within synthetic polymeric nanocapsules.[74] Depending on the loading concentration, encapsulation of ICG within the confined nanoenvironment of the virions may induce different states of aggregation, resulting in spectral shifts of the peak values. The fluorescence spectrum of OVGs resembles that of nonencapsulated ICG (Figure 2c), albeit at lower emission levels in the 755−820-nm spectral band. A similar reduction in fluorescent emission levels has been reported for PLGA constructs encapsulating ICG[75] and may be attributed to the quenching induced by interaction of ICG with the CP subunits.

To validate the interaction between ICG and BMV CP subunits, nonencapsulated ICG (775 Da) was dialyzed against the reassembly buffer in the presence or absence of the disassociated BMV CP subunits (MW = 3.6 MDa) for three days using a dialysis membrane with cut-off MW < 14 kDa. Absorption (Figure 3a) and fluorescence

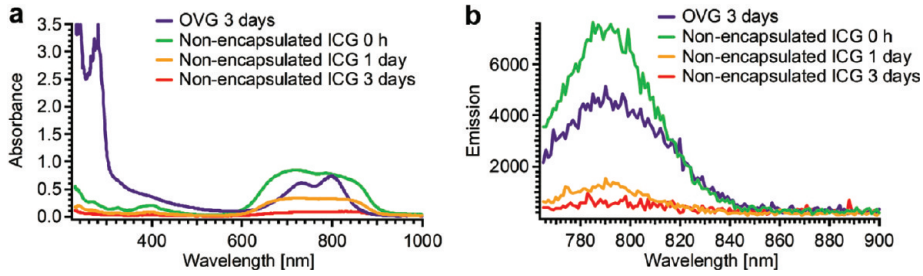

Figure 3. Optical spectra to confirm interaction between ICG and BMV CP units to form self-assembled OVGs. Panels (a) and (b) represent the respective optical absorption and fluorescence spectra of the BMV buffer solution containing free (nonencapsulated) ICG obtained immediately, one day, and three days postdialysis in the absence of CP subunits. OVGs were constructed from an ICG concentration of 10 μg mL^{-1} in BMV suspension buffer solution and using ϕ = 400.

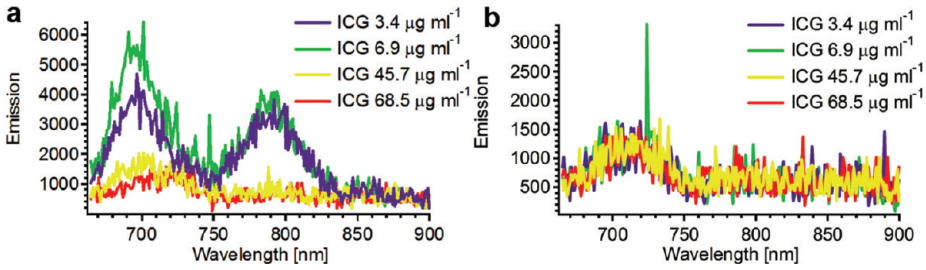

Figure 4. Fluorescence spectra to confirm encapsulation of ICG into self-assembled OVGs. Panels (a) and (b) correspond respectively to the fluorescence spectra of nonencapsulated ICG and OVGs in response to diluting the free ICC concentration, or the OVGs molarity by progressively increasing the volume of the BMV suspension buffer solution. Fluorescence spectra in panels (a) and (b) were obtained in response to 650-nm excitation wavelength. OVGs were constructed from an ICG concentration of 68.5 μg mL^{-1} in BMV suspension buffer solution and using ϕ = 10.

(Figure 3b) spectra of the BMV buffer solution were acquired immediately, one day, and three days postdialysis. Both absorption and fluorescence emission of ICG in the absence of CP subunits were almost completely diminished by three days, indicating that free ICG had diffused through the dialysis membrane.

In the presence of CP subunits, the self-assembled OVGs could not diffuse through the dialysis membrane as evidenced by the absorption and fluorescence spectra. Specifically, the absorption spectrum (Figure 3a), obtained at three days postdialysis, features the characteristics UV and NIR absorption by the CP and ICG, respectively, indicating that ICG interacted with the CP subunits to form self-assembled OVGs. Similarly, the corresponding fluorescence spectrum in Figure 3b features the monomeric emission peak to indicate successful interaction between ICG and CP subunits. Remarkably, despite (T = 1)-like symmetry, OVG remained optically active even after three days of dialysis at pH = 4.8, indicating a strong electrostatic interaction between ICG and BMV subunits to retain the ICG within OVGs.

To further verify that ICG was encapsulated into OVGs, and not localized on the surface, we performed a serial dilution experiment where the volume of BMV suspension buffer solution was progressively increased to dilute the free ICG concentration, or the OVGs molarity. The quenched fluorescence signal when using initial high ICG concentrations (45.7 and 68.5 μg mL^{-1}) was recovered in response to increased amount of solvent such that both the dimeric and monomeric emission peaks were observed (Figure 4a). This result indicated that the aggregation states of free ICG varied with changes in the solvent volume to induce changes in the fluorescence emission characteristics. With respect to OVGs, increasing the buffer volume did not alter the fluorescence emission signals (Figure 4b). This result indicated that the ICG was within OVG core and shielded from changes in the external solution environment that would have otherwise altered its fluorescence emission properties.

To examine the effect of physiological temperature on optical stability of OVGs, we incubated nonencapsulated ICG and OVGs at 37 °C for up to 3 h in BMV suspension buffer solution. With increased incubation time, optical absorption of nonencapsulated ICG progressively became broadened over the 600−900-nm spectral range, with the monomeric and dimeric and monomeric peaks becoming nearly indistinguishable (Figure 5a). In contrast, OVGs maintained their overall NIR optical absorption spectral characteristics with distinguishable dimeric and monomeric peaks at 3 h of incubation at 37 °C (Figure 5b).

Absorbance values of nonencapsulated ICG and OVGs, normalized to their respective values at the dimeric wavelengths of 709 and 733 nm, are shown in Figure 5c. While the normalized absorbance value of OVGs is reduced by ~15% at 3 h of incubation at 37 °C, it is actually the nonencapsulated ICG that experiences a more dramatic reduction in its optical stability. Specifically, a 20% reduction in absorbance was observed after

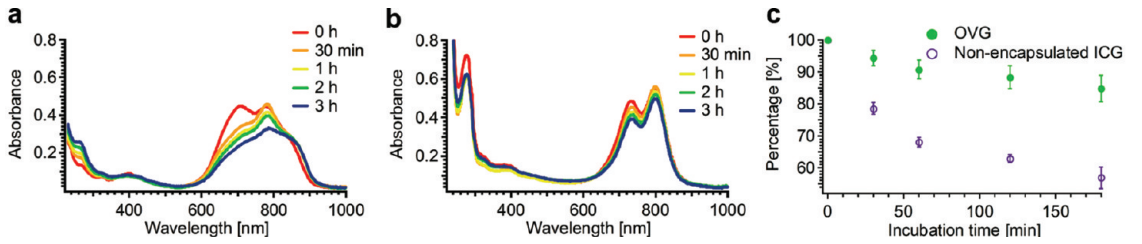

Figure 5. Effect of physiological temperature (37 °C) on the optical stability of OVGs. Optical absorption spectra of nonencapsulated (a), and OVGs (b) incubated for various time intervals. In panel (c), the mean (n = 4) absorbance values as a function of incubation time for nonencapsulated ICG and OVGs, normalized to their respective dimeric wavelengths of 709 and 733 nm, are presented. Error bars represent standard deviations. OVGs were constructed from an ICG concentration of 10 μg mL^{-1} in BMV suspension buffer solution and using ϕ = 40.

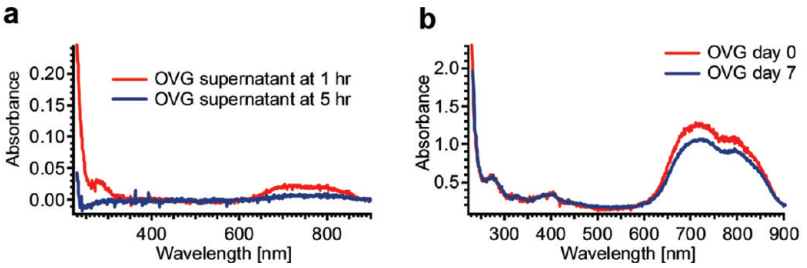

Figure 6. Physical stability of OVGs. In panel (a), optical absorption spectra of the supernatant collected at 1 and 5 h post OVG construction are presented. OVGs were constructed from an ICG concentration of 7 μg mL^{-1} in BMV buffer solution and using ϕ = 4. In panel (b), the absorbance spectra of OVGs immediately and after 7 days of storing them in BMV suspension buffer solution at 4 °C and in the dark are presented. OVG were constructed from an ICG concentration of 23.4 μg mL^{-1} in BMV suspension buffer solution and using ϕ = 4.

30 min of incubation. By 3 h, the absorbance value was diminished by 50%. When confined within OVGs, the mobility of the negatively charged ICG is likely hindered by its electrostatic attractions with the positively charged CP subunits, which immobilize the ICG molecules sufficiently enough to render them invulnerable to random changes in vibrational and translational states that occur at elevated temperatures.

To investigate the physical stability of the CP subunits and their effectiveness in encapsulating and retaining ICG, we optically analyzed the supernatant. Specifically, immediately and four hours post OVG construction, we performed high speed centrifugation (90k rpm) of the BMV suspension buffer solution containing the OVGs for one hour and subsequently, collected the supernatant. Spectra of these supernatants, corresponding to one and five hours post OVG construction, showed nearly zero absorbance in 600−900-nm NIR range, indicating that there was no ICG leakage from OVGs into the supernatant (Figure 6a). Spectrum of the supernatant at five hours post construction also showed very minimal absorbance values in the UV range, which indicated that nearly all the CP subunits were utilized in constructing the OVGs and remained intact on OVGs.

We also compared the absorbance spectrum of the OVGs immediately after construction with that obtained at 7 days postconstruction (Figure 6b). There were no differences in the UV absorbance values, suggesting that the CP subunits remained structurally intact over 7 days. While the overall shape of the NIR absorption spectrum in the 600−900-nm range remained nearly intact at 7 days, there was a reduction in the absorbance values (*e.g.* ∼20% at 700 nm), which may be attributed to some ICG leakage or degradation at 7 days.

To investigate the effectiveness of OVGs as nanoprobes for optical imaging, we incubated normal human bronchial epithelial (HBE) cells with OVGs for 3 h (Figure 7). Confocal fluorescence images (Figure 7, panels (e) and (f)) show that OVGs are internalized by the HBE cells and localized to the periphery of the nucleus, confirming the ability of OVGs as effective nanoprobes for intracellular imaging. OVG internalization may be the result of nonspecific endocytosis or a specific cell-surface protein interaction. For example, it has been reported that mammalian cells, including endothelial cells, internalize CPMV *via* a surface-expressed form of vimentin, a cytoskeletal protein.[38]

We also investigated the viability of HBE cells after 3 h of incubation with OVGs using propidium iodide (PI) applied at 20 μg mL^{-1}. PI molecules penetrate through the impaired membrane of dead cells to stain the nucleus. Nonviable cells were differentiated from live cells by detecting the red fluorescence (>615 nm) emanating from the nucleus. Over 90% of HBE cells remained viable after 3 h of incubation with OVGs (Figure 8, panels (c) and (d)) with no statistically significant differences in percentage cell viability among untreated cells (Figure 8, panel (a)), and cells treated with free ICG (Figure 8, panel (b)), and OVGs (One-way ANOVA, p-value <0.05).

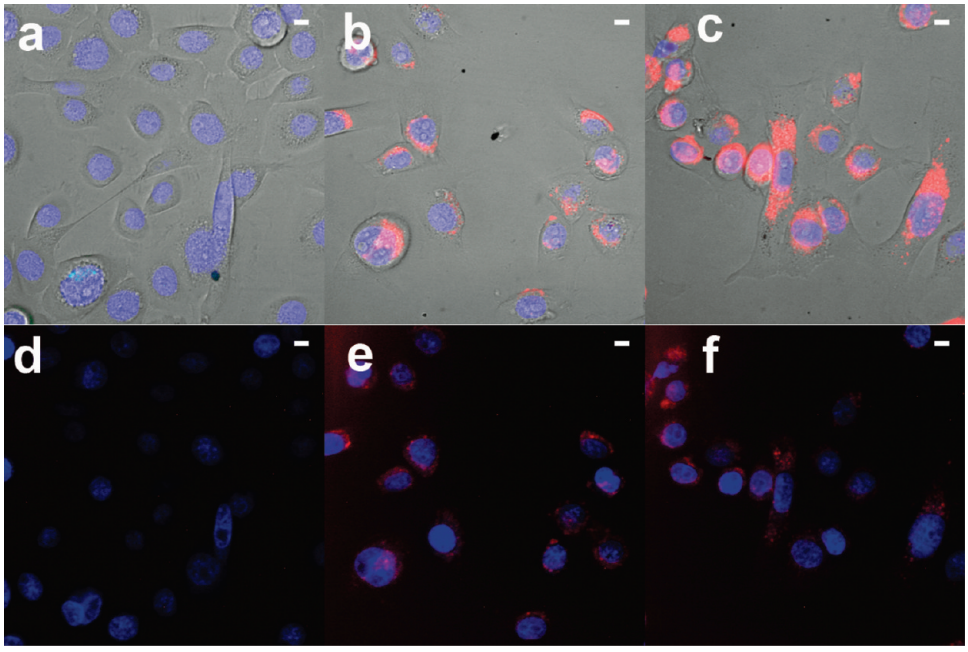

Figure 7. Optical images of HBE cells without and with exposure to OVGs. Merged bright-field and false-color full-field transmission fluorescent images are presented in panels (a−c). Panel (a) corresponds to cells without exposure to OVGs. Panels (b) and (c) correspond to cells incubated with OVGs for 3 h at 37 °C, with OVGs constructed using respective ICG buffer solution concentrations of 10 and 143 μg mL^{-1}. We used $\phi = 4$ to construct the OVGs in both cases. Panels (d−f) are confocal fluorescent images corresponding to the same fields of view as those presented in panels (a−c), respectively. Cells nuclei (represented by the blue color) were stained by 4′,6-diamidino-2-phenylindole (DAPI) to identify them as spatial references within the cells. The red color represents the ICG fluorescence signal from the OVGs. The scale bar is 10 μm in all panels.

To our knowledge, there is no prior application of plant viruses, or constructs derived from plant viruses, in humans. However, in a recent study, the toxicity of the CPMV was investigated in mice.[76] Histological examinations of various organs revealed no pathological changes. Specific detection of apoptotic cells in liver, spleen, lung, kidneys, and heart was not observed.

In another study, the biodistribution of cowpea protein cages was investigated in mice.[77] There was ≈65% elimination of protein cages through the urine and feces at 24 h post tail vein injection of naïve and immunized mice. The investigators reported no overt toxicity after a single injection, and indicated that protein cages may serve as safe, biocompatible, nanoplatforms for applications in medicine. These studies are extremely encouraging to motivate further development of OVGs for *in vivo* and clinical applications. In contrast, some synthetic polymeric materials are reported to activate inflammatory or immunological responses.[78,79]

OVGs may be tailored to identify the biomarkers of a particular disease by further surface functionalization using specific antibodies or other targeting moieties. Therefore, they may serve as a multifunctional platform for site-specific optical imaging and as a phototherapeutic material that will elicit a photothermal or a photooxidative response when irradiated by laser light. Other potential therapeutic schemes may capitalize on the addressability of specific residues on the CP subunits to attach therapeutic agents to surfaces of OVGs. Since the fluorophore is embedded within the OVGs, it remains shielded from the external environment to potentially make the interaction of the probe with cells independent of fluorophore type.

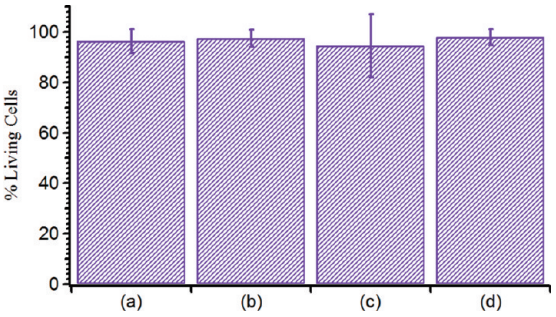

Figure 8. Effect of OVGs on viability of HBE cells. Panels (a) and (b) correspond to percentage of living cells without any treatment, and treated with free ICG (10 μg mL^{-1}), respectively. Panels (c) and (d) correspond to the percentage of living cells treated with OVGs constructed using ICG buffer solution concentrations of 10 and 143 μg mL^{-1} respectively. In both OVG-treated cases, we used $\phi = 4$ to construct the OVGs. Each panel represents the mean percentage value based on analysis of at least 170 cells with vertical error bars as the standard deviation.

The phototherapeutic and targeting potentials of a viral-based nanoconstruct was recently demonstrated using the bacteriophage MS2 whose interior surface was modified with a porphyrin agent capable of generating cytotoxic singlet oxygen in response to 415-nm irradiation wavelength, corresponding to the Soret band of the porphyrin.[80] The exterior surface was decorated with a modified DNA aptamer demonstrated to bind

tyrosine kinase 7 receptors. This dual-surface modified bacteriophage was found to be specific to Jurkat leukemia T cells and able to destroy them after 20 min of irradiation.

In addition to their fluorescent imaging capability as demonstrated here, OVGs can potentially be used as optical contrast agents for photoacoustic imaging or in combination with scattering-based imaging methods such as OCT to serve as a multimodal imaging probe. Our ongoing activities include studies aimed at characterizing the immunogenicity of OVGs and their interactions with phagocytic cells, investigating the biodistribution of OVGs in animal models, providing structural enhancements to incorporate targeting moieties for recognition of specific biomarkers of disease, and endowing therapeutic capabilities that use both drugs and photoirradiation approaches.

SUMMARY

We have demonstrated successful construction of an optically active hybrid nanomaterial composed of BMV capsid protein subunits encapsulating the organic near-infrared chromophore, ICG. These constructs are highly monodispersed, and demonstrate a high degree of physical and optical stability. Our *in vitro* studies show that OVGs can be used for intracellular optical imaging without compromising the cell viability. They may serve as a potentially nontoxic multifunctional nanoplatform for site-specific optical imaging, and therapy of various diseases.

METHODS

TEM Imaging and Diameter Measurements. Viral particle samples were placed onto 400-mesh carbon-Formvar grids (01814-F, Ted Pella Inc., Redding, CA) for 7 min. The grids were rinsed with water, wicked dry, and stained with a 1−2% uranyl acetate for 7 min. Samples were viewed at 300 kV using a Philips CM300 TEM system at 19,500−51,000× magnification. Images were collected as 1024 pixels × 1024 pixels, 14-bit gray scale Gatan Digital Micrograph 3 (DM3) files using a Gatan 794 CCD multiscan camera, and converted into 8-bit gray scale TIF files.

To measure the diameter of BMVs, VGs, and OVGs, TEM images were analyzed with the Image J program. The size scale was calibrated against a known 20-nm scale bar imaged by TEM. Approximately, 100−700 particles were analyzed to determine the size distribution, mean, and standard deviation of BMVs, VGs, and OVGs.

ζ-Potential Measurements. The ζ-potential distributions for BMV, VGs, and OVGs were obtained in deionized water within a visibly clear disposable zeta cell (DTS 1060C, Malvern, Worcestershire, UK) by a zeta potential analyzer (Malvern Zetasizer nano, Worcestershire, UK).

Spectroscopy. Absorbance spectra (230−1000 nm) were obtained using UV−vis spectrometer (Cary 50, Varian Inc.). NIR fluorescence spectra (750−900 nm) were obtained using a fluorescence spectrophotometer (Fluorolog, Horiba-Jobin-Yvon, Inc.)

Cell Culturing and Fluorescence Microscopy. Immortalized normal human bronchial epithelial (HBE4-E6/E7) cells were purchased from American Type Culture Collection (ATCC), and subcultured in LHC-9 serum free medium (Invitrogen, #12680-013) with 10 ng mL^{-1} cholera toxin. Cells were seeded into a chambered coverglass at density of ~1.12 × 106 mL^{-1} overnight, and subsequently incubated with OVGs for 3 h. After incubation, cells were washed with fresh LHC-9 medium three times before final placement in LHC-9 medium prior to imaging. Nuclei were stained by 4′,6-diamidino-2-phenylindole (DAPI). Fluorescent images were collected using a confocal microscope system (Atto Biosciences, Rockville, MD) equipped with visible and NIR excitation (740 ± 35 nm), and emission (>780 nm) filters (Chroma Technology, Bellows Falls, VT). Cells were maintained at 37 °C and supplied with 5% CO_2 during imaging. Exposure times of 0.23, 1, and 10 s were used for bright-field, fluorescence transmission, and confocal fluorescence imaging, respectively.

Acknowledgment. This work was supported by Bourns College of Engineering and the Bioengineering Center at University of California, Riverside (UCR). We are grateful for the support provided by the Central Facility for Advanced Microscopy and Microanalysis (CFAMM) at UCR in obtaining the TEM images. We also thank Ms. D. Mathews in the Plant Pathology and Microbiology Department for assistance with sucrose gradient fragmentation experiments. B.A.dedicates this paper to the memory of his mother, M. G. Kashani, who lost her life to ovarian cancer on June 11, 2010.

Supporting Information Available: Description of the detailed protocol to construct the OVGs; data showing the effects of CP:ICG concentration ratio (ϕ) and ICG concentration on optical characteristics of OVGs; role of ϕ in formation of OVGs and loading efficiency of ICG; TEM images at 11 days post-assembly; and sucrose gradient sedimentation results. This material is available free of charge *via* the Internet at http://pubs.acs.org.

REFERENCES AND NOTES

1. Nie, S. M.; Xing, Y.; Kim, G. J.; Simons, J. W. Nanotechnology Applications in Cancer. *Annu. Rev. Biomed. Eng.* **2007,** *9*, 257–288.
2. Galanzha, E. I.; Shashkov, E. V.; Kelly, T.; Kim, J. W.; Yang, L. L.; Zharov, V. P. *In Vivo* Magnetic Enrichment and Multiplex Photoacoustic Detection of Circulating Tumour Cells. *Nat. Nanotechnol.* **2009,** *4*, 855–860.
3. Tam, J. M.; Tam, J. O.; Murthy, A.; Ingram, D. R.; Ma, L. L.; Travis, K.; Johnston, K. P.; Sokolov, K. V. Controlled Assembly of Biodegradable Plasmonic Nanoclusters for Near-Infrared Imaging and Therapeutic Applications. *ACS Nano* **2010,** *4*, 2178–2184.
4. Choi, H. S.; Liu, W.; Liu, F.; Nasr, K.; Misra, P.; Bawendi, M. G.; Frangioni, J. V. Design Considerations for Tumour-Targeted Nanoparticles. *Nat. Nanotechnol.* **2010,** *5*, 42–47.
5. Lee, Y. E. K.; Smith, R.; Kopelman, R. Nanoparticle PEBBLE Sensors in Live Cells and *in Vivo*. *Annu. Rev. Anal. Chem.* **2009,** *2*, 57–76.
6. le Masne de Chermont, Q. L.; Chaneac, C.; Seguin, J.; Pelle, F.; Maitrejean, S.; Jolivet, J. P.; Gourier, D.; Bessodes, M.; Scherman, D. Nanoprobes with Near-Infrared Persistent Luminescence for *in Vivo* Imaging. *Proc. Natl. Acad. Sci. U.S.A.* **2007,** *104*, 9266–9271.
7. Gao, X.; Shivang, R., D. Quantum Dots for Cancer Molecular Imaging. *Adv. Exp. Med. Biol.* **2007,** *620*, 57–73.
8. Smith, B. R.; Cheng, Z.; De, A.; Koh, A. L.; Sinclair, R.; Gambhir, S. S. Real-Time Intravital Imaging of RGD-Quantum Dot Binding to Luminal Endothelium in Mouse Tumor Neovasculature. *Nano Lett.* **2008,** *8*, 2599–2606.
9. Kim, S.; Lim, Y. T.; Soltesz, E. G.; De Grand, A. M.; Lee, J.; Nakayama, A.; Parker, J. A.; Mihaljevic, T.; Laurence, R. G.;

Dor, D. M.; *et al.* Near-Infrared Fluorescent Type II Quantum Dots for Sentinel Lymph Node Mapping. *Nat. Biotechnol.* **2004,** *22*, 93–97.
10. Shiohara, A.; Hoshino, A.; Hanaki, K.; Suzuki, K.; Yamamoto, K. On the Cytotoxicity Caused by Quantum Dots. *Microbiol. Immunol.* **2004,** *48*, 669–675.
11. Derfus, A. M.; Chan, W. C. W.; Bhatia, S. N. Probing the Cytotoxicity of Semiconductor Quantum Dots. *Nano Lett.* **2004,** *4*, 11–18.
12. Lovric, J.; Bazzi, H. S.; Cuie, Y.; Fortin, G. R.; Winnik, F. M.; Maysinger, D. Differences in Subcellular Distribution and Toxicity of Green and Red Emitting CdTe Quantum Dots. *J. Mol. Med.* **2005,** *83*, 377–385.
13. Fischer, H. C.; Chan, W. C. W. Nanotoxicity: The Growing Need for *in Vivo* Study. *Curr. Opin. Biotechnol.* **2007,** *18*, 565–571.
14. Zhang, Y. B.; Chen, W.; Zhang, J.; Liu, J.; Chen, G. P.; Pope, C. *In Vitro* and *in Vivo* Toxicity of CdTe Nanoparticles. *J. Nanosci. Nanotechnol.* **2007,** *7*, 497–503.
15. Guo, R.; Zhang, L.; Qian, H.; Li, R.; Jing, X.; Liu, B. Multifunctional Nanocarriers for Cell Imaging, Drug Delivery, and Near-IR Photothermal Therapy. *Langmuir* **2010,** *20*, 5428–5434.
16. Hirsch, L. R.; Stafford, R. J.; Bankson, J. A.; Sershen, S. R.; Rivera, B.; Price, R. E.; Hazle, J. D.; Halas, N. J.; West, J. L. Nanoshell-Mediated Near-Infrared Thermal Therapy of Tumors under Magnetic Resonance Guidance. *Proc. Natl. Acad. Sci. U.S.A.* **2003,** *100*, 13549–13554.
17. Day, E. S.; Morton, J. G.; West, J. L. Nanoparticles for Thermal Cancer Therapy. *J. Biomech. Eng.* **2009,** *131*, 074001.
18. Zhang, Y.; Yu, J.; Birch, D. J.; Chen, Y. Gold Nanorods for Fluorescence Lifetime Imaging in Biology. *J. Biomed. Opt.* **2010,** *15*, 020504.
19. McLaughlan, J. R.; Roy, R. A.; Ju, H.; Murray, T. W. Ultrasonic Enhancement of Photoacoustic Emissions by Nanoparticle-Targeted Cavitation. *Opt. Lett.* **2010,** *35*, 22127–2129.
20. Chanda, N.; Shulka, R.; Zambre, A.; Mekapothula, S.; Kulkarni, R. R.; Katti, K.; Bhattacharyya, K.; Feng, G. M.; Casteel, S. W.; Boote, E. J.; *et al.* An Effective Strategy for the Synthesis of Biocompatible Gold Nanoparticles Using Cinnamon Phytochemicals for Phantom CT Imaging and Photoacoustic Detection of Cancerous Cells. *Pharm. Res.* 2010, DOI: 10.1007/s11095-010-0276-6.
21. Gobin, A. M.; Lee, M. H.; Halas, N. J.; James, W. D.; Drezek, R. A.; West, J. L. Near-Infrared Resonant Nanoshells for Combined Optical Imaging and Photothermal Cancer Therapy. *Nano Lett.* **2007,** *7*, 1929–1934.
22. Lu, W.; Huang, Q.; Ku, G.; Wen, X.; Zhou, M.; Guzatov, D.; Brecht, P.; Su, R.; Oraevsky, A.; Wang, L. V.; *et al.* Photoacoustic Imaging of Living Mouse Brain Vasculature Using Hollow Gold Nanospheres. *Biomaterials* **2010,** *31*, 2617–2626.
23. Manchester, M.; Singh, P. Virus-Based Nanoparticles (VNPs): Platform Technologies for Diagnostic Imaging. *Adv. Drug Delivery Rev.* **2006,** *58*, 1505–1522.
24. Destito, G.; Schneemann, A.; Manchester, M., Biomedical Nanotechnology Using Virus-Based Nanoparticles. In *Viruses and Nanotechnology*, Springer-Verlag: Berlin, 2009; Vol. 327, pp 95−122.
25. Singh, P.; Gonzalez, M. J.; Manchester, M. Viruses and Their Uses in Nanotechnology. *Drug Dev. Res.* **2006,** *67*, 23–41.
26. Singh, R.; Kostarelos, K. Designer Adenoviruses for Nanomedicine and Nanodiagnostics. *Trends Biotechnol.* **2009,** *27*, 220–229.
27. Brennan, F. R.; Jones, T. D.; Hamilton, W. D. O. Cowpea Mosaic Virus as a Vaccine Carrier of Heterologous Antigens. *Mol. Biotechnol.* **2001,** *17*, 15–26.
28. Tanaka, T.; Kuroki, M.; Hamada, H.; Kato, K.; Kinugasa, T.; Shibaguchi, H.; Zhao, J.; Kuroki, M. Cancer-Targeting Gene Therapy Using Tropism-Modified Adenovirus. *Anticancer Res.* **2007,** *27*, 3679–3684.
29. Guo, Z. S.; Thorne, S. H.; Bartlett, D. L. Oncolytic Virotherapy: Molecular Targets in Tumor-Selective Replication and Carrier Cell-Mediated Delivery of Oncolytic Viruses. *Biochim. Biophys. Acta Rev. Cancer* **2008,** *1785*, 217–231.
30. Dixit, S. K.; Goicochea, N. L.; Daniel, M. C.; Murali, A.; Bronstein, L.; De, M.; Stein, B.; Rotello, V. M.; Kao, C. C.; Dragnea, B. Quantum Dot Encapsulation in Viral Capsids. *Nano Lett.* **2006,** *6*, 1993–1999.
31. Chen, C.; Daniel, M. C.; Quinkert, Z. T.; De, M.; Stein, B.; Bowman, V. D.; Chipman, P. R.; Rotello, V. M.; Kao, C. C.; Dragnea, B. Nanoparticle-Templated Assembly of Viral Protein Cages. *Nano Lett.* **2006,** *6*, 611–615.
32. Goicochea, N. L.; De, M.; Rotello, V. M.; Mukhopadhyay, S.; Dragnea, B. Core-like Particles of an Enveloped Animal Virus Can Self-Assemble Efficiently on Artificial Templates. *Nano Lett.* **2007,** *7*, 2281–2290.
33. Huang, X. L.; Bronstein, L. M.; Retrum, J.; Dufort, C.; Tsvetkova, I.; Aniagyei, S.; Stein, B.; Stucky, G.; McKenna, B.; Remmes, N.; *et al.* Self-Assembled Virus-like Particles with Magnetic Cores. *Nano Lett.* **2007,** *7*, 2407–2416.
34. Brumfield, S.; Willits, D.; Tang, L.; Johnson, J. E.; Douglas, T.; Young, M. Heterologous Expression of the Modified Coat Protein of Cowpea Chlorotic Mottle Bromovirus Results in the Assembly of Protein Cages with Altered Architectures and Function. *J. Gen. Virol.* **2004,** *85*, 1049–1053.
35. Allen, M.; Bulte, J. W. M.; Liepold, L.; Basu, G.; Zywicke, H. A.; Frank, J. A.; Young, M.; Douglas, T. Paramagnetic Viral Nanoparticles as Potential High-Relaxivity Magnetic Resonance Contrast Agents. *Magn. Reson. Med.* **2005,** *54*, 807–812.
36. Anderson, E. A.; Isaacman, S.; Peabody, D. S.; Wang, E. Y.; Canary, J. W.; Kirshenbaum, K. Viral Nanoparticles Donning a Paramagnetic Coat: Conjugation of MRI Contrast Agents to the MS2 Capsid. *Nano Lett.* **2006,** *6*, 1160–1164.
37. Koudelka, K. J.; Rae, C. S.; Gonzalez, M. J.; Manchester, M. Interaction between a 54-kilodalton Mammalian Cell Surface Protein and Cowpea Mosaic Virus. *J. Virol.* **2007,** *81*, 1632–1640.
38. Koudelka, K. J.; Destito, G.; Plummer, E. M.; Trauger, S. A.; Siuzdak, G.; Manchester, M. Endothelial Targeting of Cowpea Mosaic Virus (CPMV) *via* Surface Vimentin. *PLoS Pathog.* **2009,** *5*, e1000417.
39. Lavelle, L.; Michel, J. P.; Gingery, M. The Disassembly, Reassembly and Stability of CCMV Protein Capsids. *J. Virol. Methods* **2007,** *146*, 311–316.
40. Destito, G.; Yeh, R.; Rae, C. S.; Finn, M. G.; Manchester, M. Folic Acid-Mediated Targeting of Cowpea Mosaic Virus Particles to Tumor Cells. *Chem. Biol.* **2007,** *14*, 1152–1162.
41. Steinmetz, N. F.; Mertens, M. E.; Taurog, R. E.; Johnson, J. E.; Commandeur, U.; Fischer, R.; Manchester, M. Potato Virus X as a Novel Platform for Potential Biomedical Applications. *Nano Lett.* **2010,** *10*, 305–312.
42. Lewis, J. D.; Destito, G.; Zijlstra, A.; Gonzalez, M. J.; Quigley, J. P.; Manchester, M.; Stuhlmann, H. Viral Nanoparticles as Tools for Intravital Vascular Imaging. *Nat. Med.* **2006,** *12*, 354–360.
43. Rao, A. L. Genome Packaging by Spherical Plant RNA Viruses. *Annu. Rev. Phytopathol.* **2006,** *44*, 61–87.
44. Yu, J.; Yaseen, M. A.; Anvari, B.; Wong, M. S. Synthesis of Near-Infrared-Absorbing Nanoparticle-Assembled Capsules. *Chem. Mater.* **2007,** *19*, 1277–1284.
45. Yaseen, M. A.; Yu, J.; Wong, M. S.; Anvari, B. Laser-Induced Heating of Dextran-Coated Mesocapsules Containing Indocyanine Green. *Biotechnol. Prog.* **2007,** *23*, 1431–1440.
46. Yaseen, M. A.; Yu, J.; Wong, M. S.; Anvari, B. Stability Assessment of Indocyanine Green within Dextran-Coated Mesocapsules by Absorbance Spectroscopy. *J. Biomed. Opt.* **2007,** *12*, 064031.
47. Yaseen, M. A.; Yu, J.; Wong, M. S.; Anvari, B. *In Vivo* Fluorescence Imaging of Mammalian Organs Using Charge-Assembled Mesocapsule Constructs Containing Indocyanine Green. *Opt. Express* **2008,** *16*, 20577–20587.
48. Yaseen, M. A.; Yu, J.; Jung, B. S.; Wong, M. S.; Anvari, B. Biodistribution of Encapsulated Indocyanine Green in Healthy Mice. *Mol. Pharm.* **2009,** *6*, 1321–1332.
49. Texier, I.; Gourtayer, M.; De Silva, A.; Guyon, L.; Djaker, N.; Josserand, V.; Neumann, E.; Bibette, J. Vinet, Cyanine-Loaded Lipid Nanoparticles for Improved *in Vivo* Fluorescence Imaging. *J. Biomed. Opt.* **2009,** *14*, 0540005.
50. Bringley, J. F.; Penner, T. L.; Wang, R. Z.; Harder, J. F.; Harrison, W. J.; Buonemani, L. Silica Nanoparticles Encapsulating

Near-Infrared Emissive Cyanine Dyes. *J. Colloid Interface Sci.* **2008,** *320*, 132–139.
51. Altinoglu, E. I.; Adair, J. H. Near Infrared Imaging with Nanoparticles. *Wiley Interdiscip. Rev. Nanomed. Nanobiotechnool.* **2010,** *2*, 461–477.
52. Frangioni, J. V. *In Vivo* Near-Infrared Fluorescence Imaging. *Curr. Opin. Chem. Biol.* **2003,** *7*, 626–634.
53. Zhao, X. X.; Fox, J. M.; Olson, N. H.; Baker, T. S.; Young, M. J. *In Vitro* Assembly of Cowpea Chlorotic Mottle Virus from Coat Protein Expressed in Escherichia coli and *in Vitro*-Transcribed Viral cDNA. *Virology* **1995,** *207*, 486–494.
54. Cuillel, M.; Berthetcolominas, C.; Timmins, P. A.; Zulauf, M. Reassembly of Brome Mosaic-Virus from Dissociated Virus: A Neutron-Scattering Study. *Eur. Biophys. J.* **1987,** *15*, 169–176.
55. van der Graaf, M.; Vanmierlo, C. P. M.; Hemminga, M. A. Solution Conformation of a Peptide Fragment Representing a Proposed RNA-Binding Site of a Viral Coat Protein Studied by 2-Dimensional NMR. *Biochemistry* **1991,** *30*, 5722–5727.
56. Belyi, V. A.; Muthukumar, M. Electrostatic Origin of the Genome Packing in Viruses. *Proc. Natl. Acad. Sci. U.S.A.* **2006,** *103*, 17174–17178.
57. Pfeiffer, P.; Herzog, M.; Hirth, L. Stabilization of Brome Mosaic-Virus. *Philos. Trans. R. Soc. Lond. B. Biol. Sci* **1976,** *276*, 99–107.
58. Li, F.; Zhang, Z. P.; Peng, J.; Cui, Z. Q.; Pang, D. W.; Li, K.; Wei, H. P.; Zhou, Y. F.; Wen, J. K.; Zhang, X. E. Imaging Viral Behavior in Mammalian Cells with Self-Assembled Capsid-Quantum-Dot Hybrid Particles. *Small* **2009,** *5*, 718–726.
59. Koo, Y. E. L.; Reddy, G. R.; Bhojani, M.; Schneider, R.; Philbert, M. A.; Rehemtulla, A.; Ross, B. D.; Kopelman, R. Brain Cancer Diagnosis and Therapy with Nanoplatforms. *Adv. Drug Delivery Rev.* **2006,** *58*, 1556–1577.
60. Dobrovolskaia, M. A.; Aggarwal, P.; Hall, J. B.; McNeil, S. E. Preclinical Studies to Understand Nanoparticle Interaction with the Immune System and its Potential Effects on Nanoparticle Biodistribution. *Mol. Pharm.* **2008,** *5*, 487–495.
61. Saxena, V.; Sadoqi, M.; Shao, J. Polymeric Nanoparticulate Delivery System for Indocyanine Green: Biodistribution in Healthy Mice. *Int. J. Pharm.* **2006,** *308*, 200–204.
62. Kim, G.; Huang, S. W.; Day, K. C.; O'Donnell, M.; Agayan, R. R.; Day, M. A.; Kopelman, R.; Ashkenazi, S. Indocyanine-Green-Embedded PEBBLEs as a Contrast Agent for Photoacoustic Imaging. *J. Biomed. Opt.* **2007,** *12*, 044020.
63. Rodriguez, V. B.; Henry, S. M.; Hoffman, A. S.; Stayton, P. S.; Li, X. D.; Pun, S. H. Encapsulation and Stabilization of Indocyanine Green within Poly(styrene-*alt*-maleic anhydride) Block-Poly(styrene) Micelles for Near-Infrared Imaging. *J. Biomed. Opt.* **2008,** *13*, 0140025.
64. Altinoglu, E. I.; Russin, T. J.; Kaiser, J. M.; Barth, B. M.; Eklund, P. C.; Kester, M.; Adair, J. H. Near-Infrared Emitting Fluorophore-Doped Calcium Phosphate Nanoparticles for *in Vivo* Imaging of Human Breast Cancer. *ACS Nano* **2009,** *2*, 2075–2084.
65. Lucas, R. W.; Kuznetsov, Y. G.; Larson, S. B.; McPherson, A. Crystallization of Brome Mosaic Virus and T=1 Brome Mosaic Virus Particles Following a Structural Transition. *Virology* **2001,** *286*, 290–303.
66. Kuznetsov, Y. G.; Malkin, A. J.; Lucas, R. W.; Plomp, M.; McPherson, A. Imaging of Viruses by Atomic Force Microscopy. *J. Gen. Virol* **2001,** *82*, 2025–2034.
67. Tang, J. H.; Johnson, J. M.; Dryden, K. A.; Young, M. J.; Zlotnick, A.; Johnson, J. E. The Role of Subunit Hinges and Molecular "Switches" in the Control of Viral Capsid Polymorphism. *J. Struct. Biol.* **2006,** *154*, 59–67.
68. Larson, S. B.; Lucas, R. W.; McPherson, A. Crystallographic Structure of the T=1 Particle of Brome Mosaic Virus. *J. Mol. Biol.* **2005,** *346*, 815–831.
69. Elrad, O. M.; Hagan, M. F. Mechanisms of Size Control and Polymorphism in Viral Capsid Assembly. *Nano Lett.* **2008,** *8*, 3850–3857.
70. Sun, J.; DuFort, C.; Daniel, M. C.; Murali, A.; Chen, C.; Gopinath, K.; Stein, B.; De, M.; Rotello, V. M.; Holzenburg, A.; Kao, C. C.; Dragnea, B. Core-Controlled Polymorphism in Virus-like Particles. *Proc. Natl. Acad. Sci. U.S.A.* **2007,** *104*, 1354–1359.
71. Zahr, A. S.; Davis, C. A.; Pishko, M. V. Macrophage Uptake of Core−Shell Nanoparticles Surface Modified with Poly(ethylene glycol). *Langmuir* **2006,** *22*, 8178–8185.
72. Alexis, F.; Pridgen, E.; Monar, L. K.; Farokhzad, O. C. Factors Affecting the Clearance and Biodistribution of Polymeric Nanoparticles. *Mol. Pharm.* **2008,** *5*, 505–515.
73. Bockstahler, L. E.; Kaesberg, P. Molecular Weight and Other Biophysical Properties of Bromegrass *Mosaic* Virus. *Biophys. J.* **1962,** *2*, 1–9.
74. Yu, J.; Javier, D.; Yaseen, M. A.; Nitin, N.; Richards-Kortum, R.; Anvari, B.; Wong, M. S. Self-Assembly Synthesis, Tumor Cell Targeting, and Photothermal Capabilities of Antibody-Coated Indocyanine Green Nanocapsules. *J. Am. Chem. Soc.* **2010,** *132*, 1929–1938.
75. Saxena, V.; Sadoqi, M.; Shao, J. Enhanced Photostability, Thermal-Stability and Aqueous-Stability of Indocyanine Green in Polymeric Nanoparticulate Systems. *J. Photochem. Photobiol., B* **2004,** *74*, 29–38.
76. Singh, P.; Prasuhn, D.; Yeh, R. M.; Destito, G.; Rae, C. S.; Osborn, K.; Finn, M. G.; Manchester, M. Biodistribution, Toxicity and Pathology of Cowpea *Mosaic* Virus Nanoparticles *in Vivo*. *J. Controlled Release* **2007,** *120*, 41–50.
77. Kaiser, C. R.; Flenniken, M. L.; Gillitzer, E.; Harmsen, A. L.; Harmsen, A. G.; Jutila, M. A.; Douglas, T.; Young, M. J. Biodistribution Studies of Protein Cage Nanoparticles Demonstrate Broad Tissue Distribution and Rapid Clearance *in Vivo*. *Int. J. Nanomed.* **2009,** *2*, 715–733.
78. Dobrovolskaia, M. A.; Mcneil, S. E. Immunological Properties of Engineered Nanomaterials. *Nat. Nanotechnol.* **2007,** *2*, 469–478.
79. Yanagisawa, R.; Takano, H.; Inoue, K. I.; Koike, E.; Sadakane, K.; Ichinose, T. Size Effects of Polystyrene Nanoparticles on Atopic Dermatitis-like Skin Lesions in NC/NGA Mice. *Int. J. Immunopathol. Pharmacol.* **2010,** *23*, 131–141.
80. Stephanopoulos, N.; Tong, G. J.; Hsiao, S. C.; Francis, M. B. Dual-Surface Modified Virus Capsids for Targeted Delivery of Photodynamic Agents to Cancer Cells. *ACS Nano* **2010,** *4*, 6014–6020.